COMMUNICATION

Check for updates

High-entropy fluorite oxide supported Pt catalysts for catalytic ammonia combustion at 1200 °C

Yankun Du,[†][a] Liang Xu,[†][ab] Bingqing Yao,[†][a] Xin He,[b] Chaokai Xu,[a] Zhiwei Dai,[b] Hongjie Wang,*[b] Ning Yan [ID] *[cd] and Qian He [ID] *[ac]

High-temperature catalytic ammonia combustion (HT-CAC) is a promising strategy for the clean and efficient utilization of energy carried by green NH₃ fuels. A key challenge lies in developing catalysts that offer high ammonia oxidation activity, excellent thermal stability, and high N₂ selectivity. In this study, we synthesized a high-entropy fluorite oxide aerogel (HEFOA) *via* supercritical drying. The enhanced chemical disorder results in a higher specific surface area and improved thermal resistance compared to its low-entropy counterpart (LEFOA). Incorporating Pt through a one-pot method yielded Pt@HEFOA, which demonstrated good catalytic activity and long-term stability during a 50-hour HT-CAC test at 1200 °C. This work opens new avenues for designing robust ammonia combustion catalysts that remain effective at extreme temperatures, which can contribute to the development of a sustainable NH₃-based hydrogen energy cycle.

New concepts

This work presents a significant advancement in high-temperature catalysis with the development of a high-entropy fluorite oxide aerogel (HEFOA)-supported Pt catalyst for catalytic ammonia combustion at 1200 °C, which is extremely challenging for conventional catalysts. Unlike conventional catalysts, which degrade under extreme conditions, the HEFOA-supported system exhibits exceptional thermal stability, maintaining structural integrity and catalytic performance. The key innovation lies in the intrinsic structural and chemical disorder of HEFOA, stemming from atomic-scale mismatches in size, mass, and charge. These inherent heterogeneities induce lattice distortion and force field fluctuations, effectively suppressing atomic diffusion and enhancing sintering resistance—a critical limitation of traditional single- or binary-oxide supports. Beyond demonstrating superior stability, this work expands the frontier of aerogel applications in catalysis, showcasing their potential as robust, high-entropy scaffolds for extreme-condition reactions. The findings open new avenues for designing next-generation high-temperature catalysts, particularly in energy-related applications where conventional metal oxides fall short.

Introduction

Ammonia, a carbon-free fuel with high energy density (3.16 kWh L⁻¹), has attracted considerable attention for its potential to decarbonize energy systems.[1] However, compared to conventional fuels, ammonia fuel suffers from poor combustibility, high NOₓ emissions, and potential slip. Catalytic ammonia combustion (CAC) offers a promising strategy to address these challenges,[2,3] but most prior studies have focused on relatively low operating temperatures, which limit the thermal potential of NH₃ combustion.[4–6] For instance, the performance of ammonia

catalytic combustion over Cu–CeOₓ catalysts below 700 °C was explored by Su *et al.*[5] Hinokuma *et al.* investigated CAC over various Cu-based and Ag-based catalysts below 900 °C and observed good low-temperature activity but could only achieve good N₂ selectivity without NH₃-slip at 600 °C generally.[7–9]

Although catalytic ammonia combustion at higher temperatures has been explored, the reported improvements remain modest.[10–12] Previously reported catalysts often show relatively high ignition temperatures and noticeable NH₃ slip, accompanied by limited N₂ selectivity. For instance, Zhou *et al.* synthesized CuOₓ@SiO₂ core–shell catalysts *via* flame spray pyrolysis that showed promising reactivity and N₂ selectivity at 1000 °C, but its cycling stability remains to be improved.[11] Noble metal catalysts such as Pt and Pd are also constrained by poor thermal robustness.[13,14] Although Pt-based catalysts are highly active, they tend to sinter at elevated temperatures, leading to reduced catalytic efficiency and increased NOₓ formation.[15]

We recently demonstrated[16] that combining atomically dispersed Pt with a thermally stable ZrO₂–Al₂O₃ support enables

a Department of Materials Science and Engineering, College of Design and Engineering, National University of Singapore, 9 Engineering Drive 1, EA #03-09, 117575, Singapore. E-mail: heqian@nus.edu.sg

b State Key Laboratory for Mechanical Behavior of Materials, Xi'an Jiaotong University, Xi'an, 710049, China. E-mail: hjwang@xjtu.edu.cn

c Centre for Hydrogen Innovations, National University of Singapore, E8, 1 Engineering Drive 3, 117580, Singapore. E-mail: ning.yan@nus.edu.sg

d Department of Chemical and Biomolecular Engineering, College of Design and Engineering, National University of Singapore, 4 Engineering Drive 4, E5 #02-29, 117585, Singapore

† These authors contributed equally.

effective high-temperature CAC (HT-CAC) at 1100 °C, achieving low ignition temperature, high N_2 selectivity, and excellent thermal stability. However, the Al_2O_3-based support in that system suffers severe surface area loss above 1100 °C, leading to catalyst deactivation.[17] Thus, the next challenge lies in developing catalysts that can further extend the HT-CAC operation window to even higher temperatures, enabling the generation of higher-quality heat from NH_3 combustion.

While various strategies have been explored to retain the surface area of conventional refractory oxides under extreme conditions,[18–20] alternative support materials with inherently superior thermal stability are also being investigated.[21] High-entropy fluorite oxides (HEFOs), a subclass of high-entropy oxides (HEOs), are composed of five or more metal cations (e.g., Ce, Zr, La, Yb, and other rare-earth elements) uniformly distributed within a single-phase fluorite-type lattice (CeO_2-like structure) at near-equimolar ratios.[22] This concept is inspired by the development of high-entropy alloys (HEAs), which have demonstrated remarkable thermal stability, sluggish diffusion, and lattice distortion effects due to their multicomponent nature.[23,24] These HEFO materials exhibit remarkable thermal stability, making them promising candidates for high-temperature applications such as thermal barrier coatings.[25,26] Furthermore, synergistic interactions among the multiple metal components optimize electronic structures, leading to outstanding catalytic performance in various reactions.[27] For instance, Xu et al.[21] prepared Pd single-atom catalysts using HEFO supports calcined at 900 °C. The resulting Pd@HEFO exhibited enhanced lattice oxygen reducibility and stable Pd–O–M species, which not only improved low-temperature CO oxidation activity but also demonstrated exceptional thermal and hydrothermal stability.[21] Similarly, Okejiri et al.[28] observed no phase segregation in the $CeHfZrSnErO_x$ support nor Pd nanoparticle sintering even after thermal treatment at 900 °C, and the catalyst exhibited better performance than Pd/CeO_2 with the same Pd loading in catalytic CO oxidation. The work by Fang et al.[29] revealed that even without Ce, high-entropy fluorite oxides retained their exceptional thermal properties.

Although HEO-based catalysts have been demonstrated to exhibit promising structural stability at elevated temperatures,[21,28] including thermochemical H_2 production[30] and catalytic methane combustion,[31] most reported catalysts operated below 900 °C. Systematic investigations into their thermal stability and catalytic performance under extreme high-temperature conditions (>1000 °C) remain scarce. In this work, we demonstrated that a high-entropy fluorite oxide aerogel (HEFOA, $Er_2(Nb_{0.2}Ta_{0.2}Y_{0.2}Yb_{0.2}Ce_{0.2})_2Ce_2O_7$) could serve as a thermally robust support for Pt, maintaining surface area and catalytic stability at temperatures as high as 1200 °C. This was inspired by our previous study, in which we determined that the compound $Er_2(Nb_{0.2}Ta_{0.2}Y_{0.2}Yb_{0.2}Ce_{0.2})_2Ce_2O_\delta$ exhibited low thermal conductivity from room temperature to 1000 °C, indicating a high degree of porosity and suggesting its potential to retain a relatively high specific surface area at elevated temperatures.[32]

Here, we prepared a new class of HT-CAC catalysts based on HEFO supports, derived from a HEFOA synthesized via a supercritical CO_2 drying method. HEFOA exhibits pronounced chemical disorder, including atomic size, mass, and charge mismatches, which induces significant lattice distortion and atomic-scale force field fluctuations. These features were reported to inhibit atomic diffusion and increase the sintering barriers.[32,33] Incorporating Pt precursors through a one-pot synthesis method yielded Pt@HEFOA, which demonstrated high catalytic activity and long-term stability in HT-CAC at 1200 °C. These findings establish Pt@HEFOA as a highly promising catalyst for ultra-high-temperature applications, offering good sintering resistance and thermal durability.

Results and discussions

Synthesis of HEFOA materials

The high-entropy fluorite oxide (HEFOA, $Er_2(Y_{0.2}Yb_{0.2}Nb_{0.2}Ta_{0.2}Ce_{0.2})_2O_7$) was synthesized via a sol–gel method, as illustrated in Fig. 1a. In a typical procedure, stoichiometric amounts of $ErCl_2 \cdot 6H_2O$ (20 mmol) along with $YCl_3 \cdot 6H_2O$, $YbCl_3 \cdot 6H_2O$, $NbCl_5$, $TaCl_5$, and $CeCl_3$ (4 mmol each) were dissolved in 100 mL of anhydrous ethanol. The mixture was continuously stirred for 12 hours at room temperature to ensure complete homogenization. Subsequently, 120 g of propylene oxide (PO) was added as a gelation agent and stirred for 3 minutes to initiate gel formation. The resulting wet gel was aged for 3 days at room temperature, followed by supercritical drying for 6 hours to remove residual solvents. Finally, the obtained xerogel was calcined in air at temperatures ranging from 500 to 1200 °C to investigate the phase evolution during HEFOA formation. To further elucidate the role of configuration entropy in enhancing sintering resistance, a low-entropy fluorite oxide aerogel (LEFOA, $Er_2Ce_2O_7$), was synthesized using an identical methodology (Fig. 1b). The HEFOA exhibited an ultralow density of $\sim$100 mg cm^{-3}, coupled with a porosity exceeding 90% (see Methods). Its exceptional lightweight nature is visually demonstrated by its ability to rest stably on a delicate leaf (Fig. S1).[34]

Fig. 2 and Fig. S2 present the scanning transmission electron microscopy (STEM) and X-ray energy-dispersive spectroscopy (XEDS) characterization results of the HEFOA-1100 sample (calcined at 1100 °C for 4 hours in air). The corresponding XEDS spectra and elemental mapping demonstrate homogeneous spatial distribution of Er, Y, Yb, Nb, Ta, Ce, and O. These results confirm the successful formation of a high-entropy fluorite oxide structure with uniform elemental mixing.

X-ray diffraction (XRD) was employed to examine the crystallization behavior of HEFOA upon calcination at varying temperatures (Fig. 3a). At 500 °C, the XRD pattern exhibited broad peaks, suggesting the formation of nanosized crystals embedded within an amorphous matrix. As the temperature increased, the peak intensities gradually intensified, reflecting enhanced crystallinity and particle growth. Upon reaching 1200 °C, eight well-defined diffraction peaks emerged, which were indexed to the (111), (200), (220), (311), (222), (400), (331), and (420) planes of a defective fluorite structure.[6] In
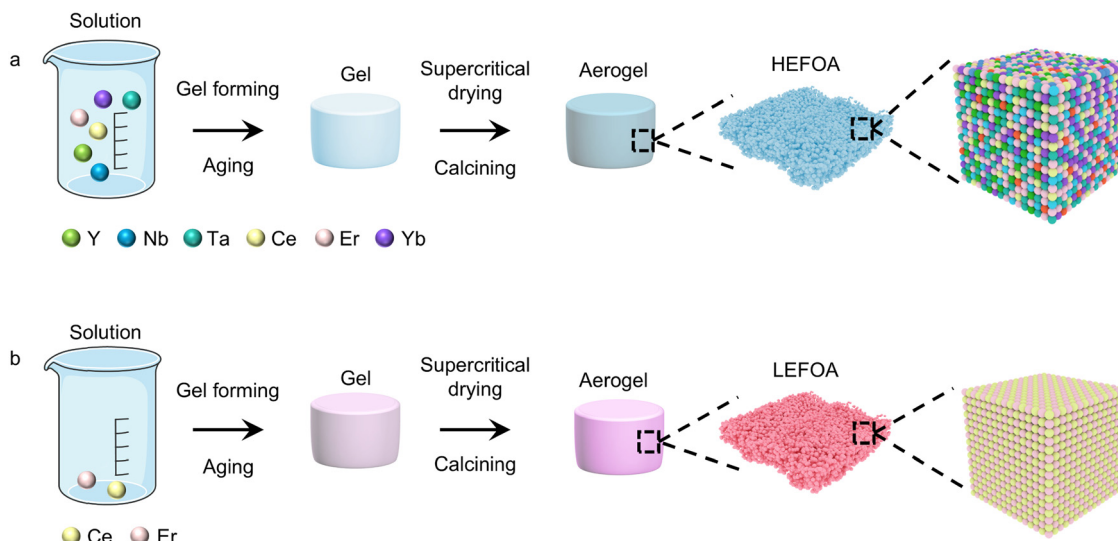
Fig. 1 The schematic synthetic routes of HEFOA (a) and LEFOA (b).

comparison, LEFOA exhibited a similar XRD evolution trend but demonstrated a higher degree of crystallinity at 500 °C (Fig. 3b). The lower crystallinity of the HEFOA $Er_2(Y_{0.2}$-$Yb_{0.2}Nb_{0.2}Ta_{0.2}Ce_{0.2})_2O_7$ compared to the LEFOA $Er_2Ce_2O_7$ can be attributed to several factors. In the low-entropy system, the high CeO_2 content provides abundant nucleation sites,

facilitating ordered grain growth even at relatively low temperatures. In contrast, the nucleation effect of Ce^{4+} in the high-entropy composition is diluted by the presence of multiple cations, making it less effective in initiating crystallization.[35] Furthermore, the significant mismatch in ionic radii among the five constituent cations leads to significant lattice
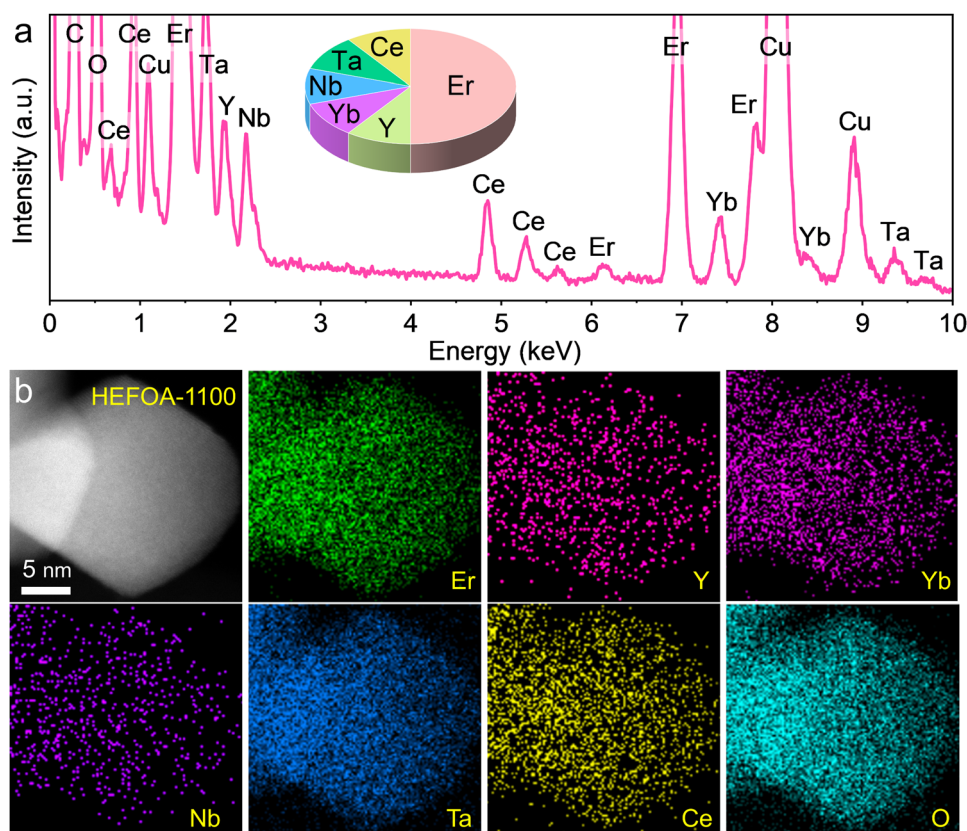

Fig. 2 STEM-XEDS analysis and elemental mapping of HEFOA materials. (a) Sum X-ED spectrum, and (b) STEM image and the corresponding elemental mappings of the HEFOA-1100 sample (after calcining for 4 hours at 1100 °C in air). Additional STEM-XEDS analysis can be found in Fig. S2.
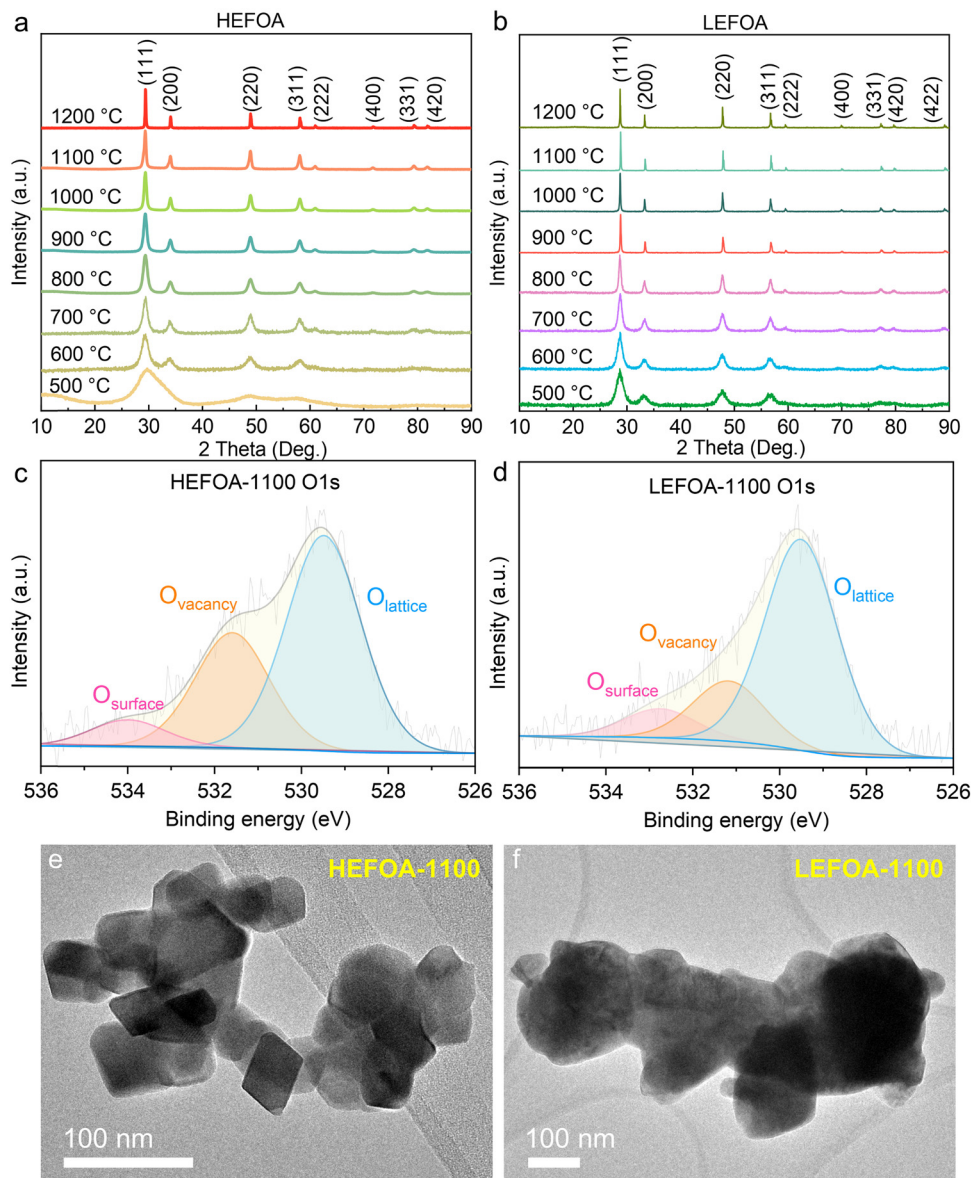
Fig. 3 Structure characterization of HEFOA and LEFOA materials. XRD patterns of (a) HEFOA and (b) LEFOA materials after calcined for 4 hours at different temperatures in air. O 1s XPS profiles of (c) HEFOA-1100 and (d) LEFOA-1100 materials. TEM images of (e) HEFOA-1100 and (f) LEFOA-1100 materials.

distortion in HEFOA. Additionally, the coexistence of multiple elements in HEFOA induces a sluggish diffusion effect, suppressing atomic mobility and hindering grain boundary migration and grain growth, especially at lower temperatures.[36,37]

The O 1s X-ray photoelectron spectroscopy (XPS) profiles of HEFOA-1100 and LEFOA-1100 are presented in Fig. 3c and d. In HEFOA-1100, the peaks observed at approximately 529.5 eV, 531.6 eV, and 534.0 eV correspond to lattice oxygen ($O_{lattice}$), oxygen vacancies ($O_{vacancy}$), and surface oxygen species (e.g., hydroxyl groups, $O_{surface}$), respectively.[38] It can be seen that the proportion of oxygen vacancies in all oxygen sites reached 32.2% in the HEFOA-1100 sample, which was significantly higher than that of 20.1% in LEFOA. This difference can be ascribed to several factors. First, the random arrangement in HEFOA introduces local strain and weakens metal–oxygen

bonds, facilitating oxygen atom detachment from the lattice, thus the configurational entropy reduces oxygen vacancy formation energy.[39,40] In addition, the mismatch in atomic radii of different metal elements induces significant lattice distortion and local strain in HEFOA.[41] The high configurational entropy enables HEOs to maintain a single-phase structure at high temperatures, inhibiting the annihilation of oxygen vacancies due to cation migration or phase transition.[42]

The average grain sizes of HEFOA and LEFOA particles, calculated using the Scherrer formula (see the Methods section for details) after calcination at different temperatures, are presented in Fig. S3. For HEFOA particles, the average grain size increased from ∼2.5 nm to 33 nm as the calcination temperature rose from 500 to 1200 °C. Notably, grain growth proceeded slowly below 900 °C but accelerated significantly

above this temperature, consistent with a liquid-assisted growth mechanism, as reported in our prior work.[43] In contrast, LEFOA particles exhibited significantly larger grain sizes under identical calcination conditions. The superior sintering resistance of HEFOA, evidenced by its higher activation energy, accounts for this difference. Transmission electron microscopy (TEM) images (Fig. 3e and f, and Fig. S4) confirm that HEFOA-1100 retains much finer particle sizes compared to LEFOA-1100. This enhanced stability can be attributed to sluggish diffusion kinetics arising from the extreme structural disorder in HEFOAs (Fig. S5). The mutual solid solution of ions with distinct radii, masses, and charges within the HEFOA lattice has led to an unprecedented increase in structural disorder.[33] This, in turn, significantly hinders mass transfer, resulting in higher sintering activation energy and enhanced high-temperature stability.

High-entropy-driven stability and sintering resistance of HEFOA

The HEFOA system possesses an exceptionally high configurational entropy ($>1.5R$), which confers superior thermodynamic stability at elevated temperatures.[37] This behavior can be quantitatively described by the Gibbs free energy equation ($\Delta G_{mix} = \Delta H_{mix} - T\Delta S_{mix}$), where the entropic term ($T\Delta S_{mix}$) becomes increasingly dominant with increasing temperature.[44] As demonstrated in Fig. 4, the calcined HEFOA exhibits significantly higher surface area and stability compared to calcined LEFOA. Notably, after calcination at 1200 °C for 4 hours in air (HEFOA-1200), the material maintains a surface area of ~ 9 m^2 g^{-1}, whereas LEFOA-1200 becomes nearly 0 m^2 g^{-1} due to significant sintering. This highlights HEFOA's potential as a robust support for high-temperature combustion reactions. Further pore size distribution analysis (Fig. 4c) reveals that HEFOA-1200 contains predominantly mesopores and macropores, while LEFOA-1200 exhibits minimal pore volume, consistent with its negligible surface area retention. The scanning electron microscopy (SEM) images of HEFOA-1200 (Fig. S6) revealed well-preserved pore structures, demonstrating its potential as a stable support material for high-temperature catalytic reactions. Thermal stability was evaluated through simultaneous thermogravimetric analysis (TGA) and differential scanning calorimetry (DSC) under atmospheric
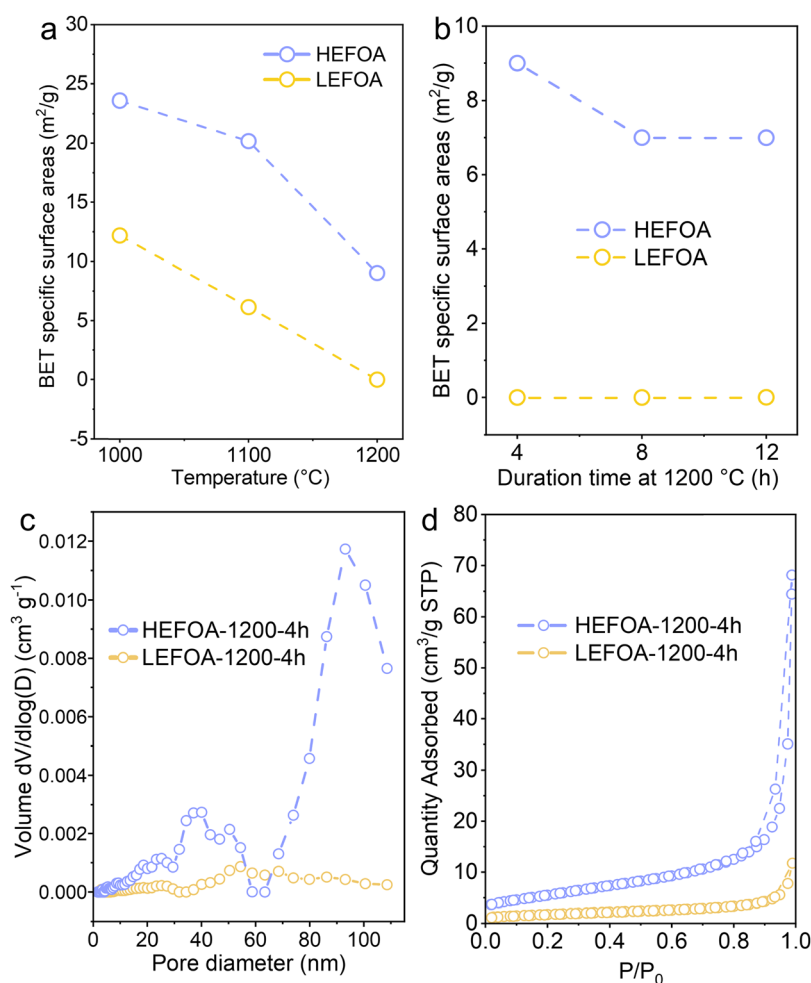

Fig. 4 The evolution of Brunauer–Emmett–Teller (BET) surface areas of HEFOA and LEFOA materials (a) after calcining at 1000, 1100, and 1200 °C for 4 hours in air, and (b) after calcining at 1200 °C for 4, 8, and 12 hours in air. The (c) pore size distributions and (d) N$_2$ adsorption/desorption isothermal of HEFOA-1200 and LEFOA-1200 materials.

conditions (Fig. S7). The TGA curve showed minimal mass loss ($<1\%$), while the DSC profile exhibited no abrupt thermal transitions between room temperature and 1200 °C, collectively confirming the material's exceptional thermal stability. Notably, a pronounced endothermic peak appeared in the 800–1200 °C range on the DSC curve, likely corresponding to intermediate phase evolution and oxygen release processes at elevated temperatures.[45]

Characterization of Pt@HEFOA and HT-CAC performance at 1200 °C

We further prepared a Pt@HEFOA catalyst and tested its performance for the high-temperature combustion of NH$_3$. Pt-based materials are commonly studied catalysts in NH$_3$ selective catalytic oxidation (NH$_3$-SCO), however, they usually struggle in deactivation due to the Pt active species aggregation

caused by elevated reaction temperatures.[46] In this work, Pt@HEFOA and Pt@LEFOA catalysts (both with a nominal Pt loading of 0.5 wt% based on our previous study[16]) were synthesized *via* a one-pot method (see the Methods section for details). The STEM high-angle annular dark-field (HAADF) image, XEDS analysis and elemental mapping (Fig. S8) identified that Pt species were uniformly dispersed in LEFOA. After incorporating Pt species and calcining at 1100 °C for 4 hours in air, Pt@HEFOA retained the high-entropy fluorite oxide structure but exhibited a slight right shift in XRD pattern compared to HEFOA-1100 (Fig. 5a and b), suggesting successful incorporation of Pt into the cation sublattice. *In situ* CO adsorption diffuse reflectance infrared Fourier transform spectroscopy (CO-DRIFTS) analysis (Fig. 5c) further confirmed the presence of Pt single atoms (absorption band at $\sim$2078 cm^{-1}) in Pt@HEFOA.[47,48] N$_2$ physisorption analysis (Fig. 5d and e)
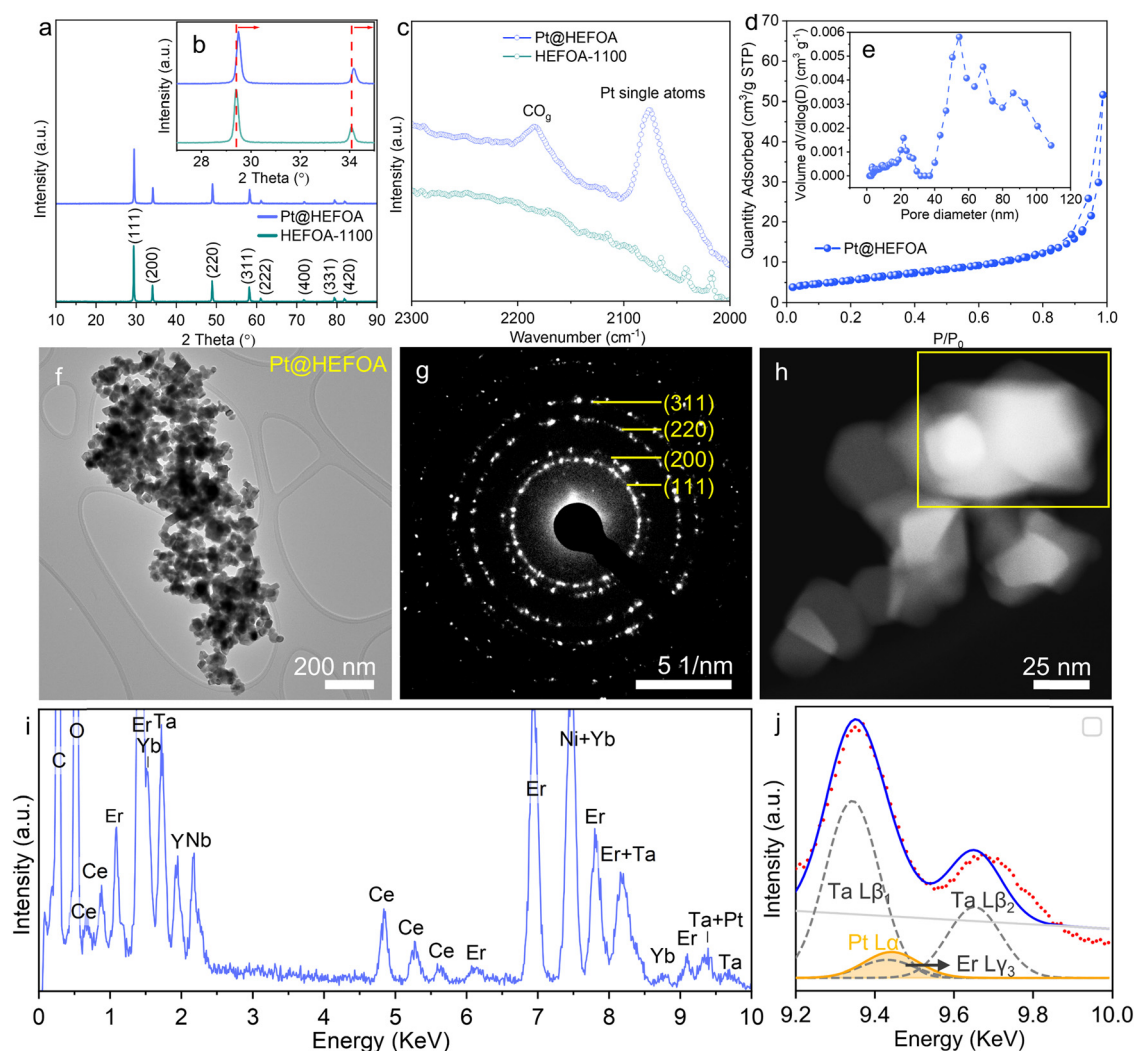

Fig. 5 Structure characterization of the catalyst after incorporating Pt (Pt@HEFOA). (a) XRD patterns of Pt@HEFOA and HEFOA-1100. (b) Enlarged view of the XRD patterns in the 2θ range of 27−35°, highlighting a slight rightward shift of the (111) and (200) peaks in Pt@HEFOA compared to HEFOA-1100. (c) *In situ* CO-DRIFTS analysis of Pt@HEFOA and HEFOA-1100. Prior to data collection, the sample was reduced in 5 vol% H$_2$/N$_2$ at 300 °C for 1 h.[49] (d) N$_2$ adsorption/desorption isotherms and (e) corresponding pore size distributions of Pt@HEFOA-1100. (f) TEM image and (g) corresponding SAED pattern of Pt@HEFOA. (h) STEM-HAADF image and (i) sum X-ED spectrum of Pt@HEFOA. (j) Sum X-ED spectrum of Pt@HEFOA in the golden rectangle area in (h).

revealed nearly identical isotherms and pore size distributions between Pt@HEFOA and HEFOA-1100, confirming that Pt incorporation had negligible impact on the material's pore structure. TEM imaging (Fig. 5f and Fig. S9) further demonstrated uniform particle size distribution, with the corresponding selected area electron diffraction (SAED) pattern aligning well with the XRD results in Fig. 5g. XEDS analysis and elemental mappings (Fig. 5h–j and Fig. S10–S12) verified the presence of Pt and the homogeneous distribution of all constituent elements (Er, Y, Yb, Nb, Ta, Ce, and O).

The catalytic performance of Pt@HEFOA and other reference materials in ammonia combustion was evaluated using a fixed-bed reactor system (Fig. S13), as illustrated in Fig. 6. Both Pt@HEFOA and Pt@LEFOA exhibited comparable catalytic activity (Fig. 6a), as evidenced by their similar 10% (T_{10}) and 90% (T_{90}) NH_3 conversion temperatures. Notably, these Pt-loaded catalysts demonstrated significantly higher activity than HEFOA, LEFOA, sand, and an empty tube.

Despite their similar activity, Pt@HEFOA and Pt@LEFOA displayed a marked difference in N_2 selectivity at 1200 °C (Fig. 6b). Specifically, Pt@HEFOA achieved an exceptional N_2 selectivity of 99.6%, whereas Pt@LEFOA yielded around 97.5%,

resulting in substantially higher NO_x emissions for the latter. Interestingly, undoped LEFOA exhibited superior N_2 selectivity compared to HEFOA, likely due to its higher oxygen vacancy content and enhanced lattice oxygen mobility of LEFOA. However, upon Pt doping, the synergistic interaction between Pt and HEFOA led to significantly improved N_2 selectivity in Pt@HEFOA. In contrast, non-catalytic ammonia combustion (represented by the empty tube) required temperatures exceeding 700 °C to achieve 90% NH_3 conversion and exhibited poor N_2 selectivity (1200 °C), thereby highlighting the critical role of catalysts in optimizing ammonia combustion reactions.

To elucidate the reaction pathway of NH_3 combustion over Pt@HEFOA, *in situ* DRIFTS experiments were conducted at 250 °C,[50–52] corresponding to around 50% NH_3 conversion. As depicted in Fig. S14, NH_3 adsorption occurred on both Lewis (L) and Brønsted (B) acid sites of Pt@HEFOA at this temperature.[53,54] Upon O_2 introduction, the Lewis-bound NH_3 species (evidenced by the band at ∼1200 cm^{-1}) were rapidly consumed, while Brønsted-bound NH_3 remained largely inert. This observation highlights the pivotal role of Lewis acid sites in facilitating low-temperature NH_3 oxidation.[55] Furthermore, two characteristic peaks emerged at ∼1415 cm^{-1} and
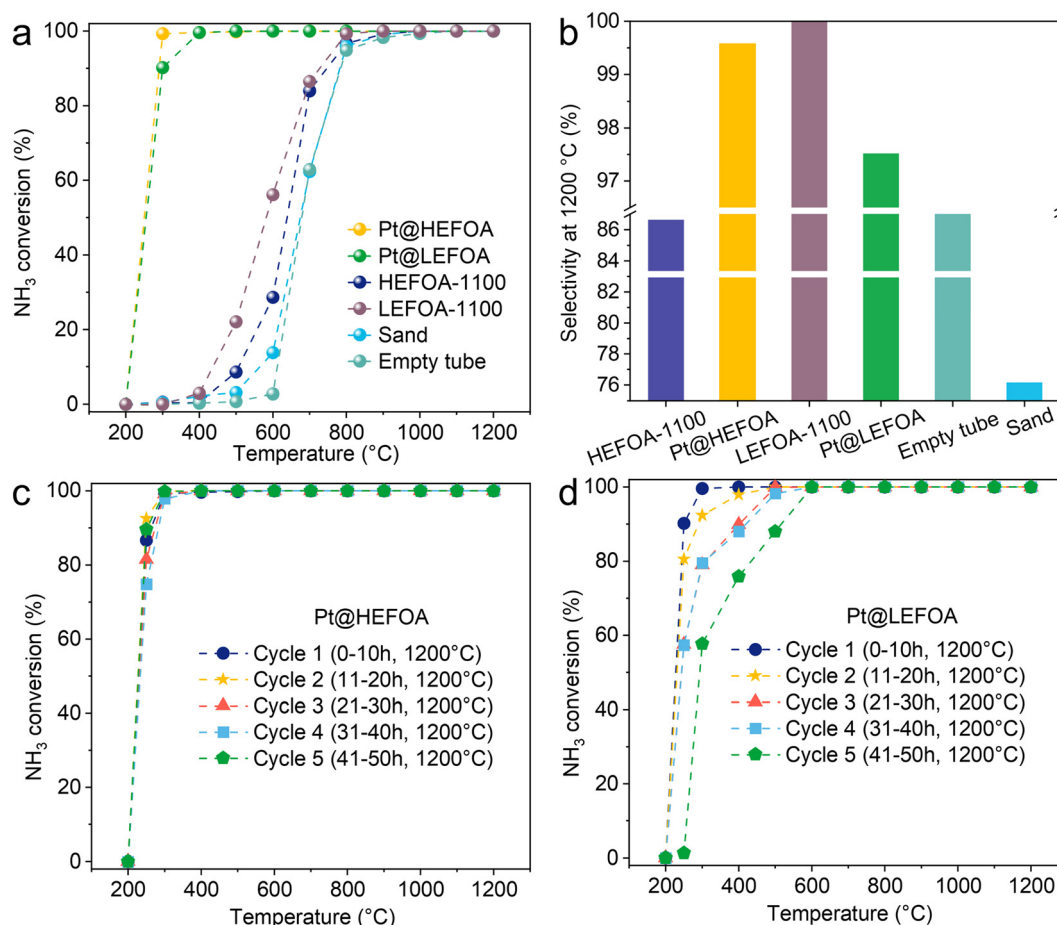

Fig. 6 HT-CAC performance of materials. (a) NH_3 conversion at different temperatures. (b) N_2 selectivity at 1200 °C. The NH_3 conversion of (c) Pt@HEFOA and (d) Pt@LEFOA during 50-hours cycle stability tests. Reaction conditions for (a)–(d): 2 vol% NH_3, 3 vol% O_2, Ar balance, 100 mL min^{-1} flow rate, W/F = 2 × 10^{-3} g min mL^{-1}, GHSV = 5500 h^{-1}.

~ 1557 cm^{-1}, assignable to monodentate and bidentate nitrite species, respectively. These spectral features align with reported CeO$_2$-based catalysts by Sun et al.,[52] suggesting the participation of an internal selective catalytic reduction (iSCR) mechanism during low-temperature NH$_3$-SCO over Pt@HEFOA.

The long-term thermal stability of the as-prepared catalysts under harsh conditions (1200 °C in HT-CAC) was evaluated. As illustrated in Fig. 6c and d, the NH$_3$ conversion profiles were monitored over a 50-hour continuous test. Pt@HEFOA exhibited outstanding stability, maintaining nearly constant NH$_3$ conversion throughout the test. The 50-hour durability test was primarily designed to compare the thermal stability of high-entropy and low-entropy supports under HT-CAC conditions. Pt@HEFOA exhibited markedly superior stability over Pt@LEFOA, and its cycling performance was comparable to our previous results in 1100 °C HT-CAC,[16] highlighting the advantage of high-entropy oxide supports in high-temperature ammonia combustion. In contrast, Pt@LEFOA displayed progressive deactivation with increasing reaction time (Fig. 6d), accompanied by a notable rise in both T_{10} and T_{90} (Fig. S15), indicative of deteriorating catalytic performance.

The in situ CO-DRIFTS spectra of fresh Pt@LEFOA, Pt@LE-FOA-50h, and Pt@HEFOA-50h are shown in Fig. S16. The fresh Pt@HEFOA and Pt@LEFOA samples exhibited similar profiles of atomically dispersed Pt species. However, after 50 hours of HT-CAC at 1200 °C, the Pt@HEFOA-50h sample retained a spectral profile similar to that of the fresh catalyst, whereas the Pt@LEFOA-50h sample displayed an additional distinct peak corresponding to Pt nanoparticles (NPs). A shoulder peak between 1900–1800 cm^{-1} was observed in the Pt@HEFOA, HEFOA-1100, and Pt@LEFOA samples (all calcined at 1100 °C). Combined with the spectra in the 1800–1300 cm^{-1} region (Fig. S17), this feature likely arises from carbonate formation due to the reaction between CO and the supports.[56] The significantly lower intensity in the 50-hour samples can be attributed to reduced surface-active oxygen species, likely caused by the decreased surface area[16] in 1200 °C HT-CAC.

These results indicate a much stronger metal–support interaction between Pt and HEFOA, which is analogous to the interaction mechanism reported by Xu et al. in their study on Pd/(CeZrHfTiLaO)$_x$ catalysts.[50] In their system, single Pd atoms were incorporated into the oxide sublattice via stable Pd–O–M (M = Ce/Zr/La) bonds, leading to significantly enhanced thermal stability compared to conventional Pd/CeO$_2$ catalysts. In our work, the enhanced Pt stability on HEFOA can similarly be attributed to the formation of strong Pt–O–M interactions, enabled by the presence of multiple, compositionally diverse cationic sites that act as robust anchoring centers. This is supported by the stable surface area of HEFOA even after prolonged high-temperature treatment (Fig. 4b), in contrast to the near-zero surface area observed for LEFOA under the same conditions. Furthermore, the high-entropy configuration of HEFOA not only provides a large number of heterogeneous coordination environments but also induces severe lattice distortion and sluggish diffusion, which together suppress Pt migration and agglomeration at elevated temperatures.

As shown in Fig. S18, the Pt@HEFOA-50h retained grain sizes in the range of 50–100 nm, showing limited growth compared to the fresh sample synthesized at 1100 °C (Fig. S12a) and demonstrating good thermal stability. XRD analysis (Fig. S19) further confirmed that the spent catalyst maintained a single-phase fluorite structure identical to the fresh catalyst (Fig. 5a). While strong SiO$_2$ peaks were observed due to the quartz sand used in the catalyst bed, the characteristic reflections of the HEFOA phase remained clearly identifiable, indicating the structural integrity of the catalyst after prolonged operation. These findings highlight Pt@HEFOA as a promising candidate for industrial HT-CAC applications, due to its superior stability under extreme thermal conditions.

Conclusions

In summary, this study demonstrates that the HEFOA support exhibits high thermal stability, retaining a functional specific surface area even after calcination at 1200 °C. The resulting Pt@HEFOA catalyst exhibits good performance in high-temperature catalytic ammonia combustion, combining high activity with increased N$_2$ selectivity. Notably, Pt@HEFOA maintains cycling stability, showing no detectable degradation after 50 hours of continuous operation at 1200 °C, exceeding the durability of reference catalysts. These results position HEFOA as a next-generation refractory support for high-temperature catalytic combustion, offering a promising pathway toward efficient and clean utilization of ammonia as a carbon-free fuel.

Methods

Materials

ErCl$_3$·6H$_2$O (99.0%), YCl$_3$·6H$_2$O (99.5%), YbCl$_3$·6H$_2$O (99.0%), and CeCl$_3$ (99.0%) were purchased from Sigma-Aldrich. Propylene oxide (PO, 99.0%), NbCl$_5$ (99.5%), H$_2$PtCl$_6$ (5 wt% in aqueous solution), and TaCl$_5$ (99.5%) were obtained by Sigma-Aldrich. All chemicals and solvents were used as received without further purification.

Preparation of HEFOA and LEFOA

For HEFOA, in a typical process, 20 mmol of ErCl$_3$·6H$_2$O and 4 mmol each YCl$_3$·6H$_2$O, YbCl$_3$·6H$_2$O, NbCl$_5$, TaCl$_5$, and CeCl$_3$ were dissolved in 100 mL of anhydrous ethanol, and stirred for 12 hours at room temperature for homogenization. Then 120 g propylene oxide were added in the solution and stirred for 3 min, forming the wet gel. After aging for 3 days at room temperature, the obtained wet gel was dried under supercritical conditions for 6 hours to remove the solvent in the wet gel. The xerogel was then calcined at temperatures ranging from 500 to 1200 °C in air by 10 °C min^{-1} to investigate the phase composition during the HEFOA formation process. The LEFOA followed the same procedure except using 20 mmol of ErCl$_3$·6H$_2$O and 20 mmol CeCl$_3$ as the precursor.

Preparation of Pt@HEFOA and Pt@LEFOA

The Pt@HEFOA was prepared *via* a similar sol–gel method. Six metal chlorides, including $ErCl_3 \cdot 6H_2O$, $YCl_3 \cdot 6H_2O$, $YbCl_3 \cdot 6H_2O$, $NbCl_5$, $TaCl_5$, and $CeCl_3$ were used as the raw materials. In a typical process, 20 mmol of $ErCl_3 \cdot 6H_2O$ and 4 mmol of the remaining chloride were dissolved in 100 mL of anhydrous ethanol, and stirred for 12 hours at room temperature for homogenization. 1 g of 8 wt% H_2PtCl_6 solution and 120 g propylene oxide (PO) were added in the solution and stirred for 3 minutes, forming the wet gel. After aging for 3 days at room temperature, the obtained wet gel was dried under supercritical conditions for 6 hours to remove the solvent in the wet gel. The xerogel was then calcined to 1100 °C in air by 10 °C min⁻¹ to obtain Pt@HEFOA catalysts. The Pt@LEFOA followed the same procedure except using 20 mmol of $ErCl_3 \cdot 6H_2O$ and 20 mmol $CeCl_3$ as the precursor.

HT-CAC reaction tests

The catalytic performance evaluation system shown in Fig. S13 mainly includes the high temperature furnace (GSL-1700X-VTφ60), calibrated mass flowrate controller (MFC, Sevenstar, D07-7D), and the mass spectrometer (MS, Hidden Analytical, HPR-20 R&D), using a 7 mm inner and 12 mm outer diameter corundum tube. MS was used to detect the gas concentration before and after the reaction. The MS system used in this study (Hiden Analytical, HPR-20 R&D) was calibrated by determining the sensitivity values of NH_3, O_2, and Ar relative to N_2, using a reference gas mixture of known composition (2 vol% NH_3, 3 vol% O_2, and 95 vol% Ar). The calibration assumes that the total gas concentration in the mixture sums to 100%. To prevent measurement errors or potential damage to the MS system from water vapor condensation, the transfer lines were tightly wrapped with heating tape maintained at 120 °C to ensure that water remained in the vapor phase throughout the measurement. Before the NH_3 catalytic combustion reaction, 200 mg catalysts and about 1000 mg quartz sand (50–70 mesh, Sigma Aldrich) were mixed evenly and then put into the quartz tube. The sand served as a thermal diluent to minimize the formation of hot spots during the highly exothermic ammonia oxidation process. The temperature rising rate during reaction is fixed at 10 °C min⁻¹, and the furnace is kept at constant temperature for 10 minutes at 200, 300, 500, 700, 900, 1100, and 1200 °C, respectively.

Test conditions: 2 vol% NH_3 (Air liquid, 99.9995%), 3 vol% O_2 by 10 vol% O_2/Ar (Air liquid, >99.9%), while using pure Ar (Air liquid) as the balance gas. The total gas flow rate was 100 mL min⁻¹ to meet a W/F_{total} of 2×10^{-3} g min$_{ml}^{-1}$, GHSV = 5500 h⁻¹. Note: GHSV in this work was calculated by the total flow rate dividing the volume of catalyst bed (about 1.1 ml), including the catalyst and sand.

Under this condition, the NH_3 conversion (λ) was calculated in the temperature range of 200–1200 °C, which was calculated using eqn (1):

$$\lambda = (C_{in} - C_{out})/C_{in} \times 100\% \tag{1}$$

where C_{in} and C_{out} refer to the NH_3 concentration of the inlet and outlet, respectively.

The selectivity of the material was calculated using eqn (2):

$$N_2 \text{ selectivity} = C_{N_2}/(C_{N_2} + 0.5C_{NO} + C_{N_2O}) \times 100\% \tag{2}$$

C is the concentration of the gas in the total flow.

While the final NO_x emissions (ppm) are calculated using eqn (3):

$$NO_x \text{ emissions} = (C_{NO} + C_{N_2O})/(C_{N_2} + C_{NO} + C_{N_2O} + C_{Ar}$$
$$+ C_{O_2} + C_{NH_3} + C_{H_2O}) \tag{3}$$

Catalyst characterizations

The porosity (P) of an aerogel is estimated based on the ratio of the measured bulk density p_b to the theoretical density p_s of the material by eqn (4):

$$P = (1 - p_b/p_s) \times 100\% \tag{4}$$

The measured bulk density p_b is based on the measured volume and mass of aerogel. The theoretical density p_s of the aerogel was calculated based on its unit cell parameters (edge lengths a, b, c and angles α, β, γ) which are typically obtained *via* X-ray diffraction. Skeletal density is defined as the solid mass divided by the framework volume (excluding pores) in eqn (5):

$$p_s = m/V = (Z \cdot M)/(N_A \cdot V) \tag{5}$$

The total molar mass M of atoms/molecules in a single unit cell based on the aerogel's composition, and Z represents the number of atoms per unit cell. Mass of a unit cell $m = (Z \cdot M)/N_A$, where N_A is Avogadro's constant, amd V is the volume of unit cell based on its parameters (edge lengths a, b, c and angles α, β, γ).

XRD patterns were collected using a Bruker D8 Advance with Cu Kα radiation from 2 theta angles of 10° to 90° with a step size of 0.02°. Different batches of HEFOAs were annealed at each temperature for 4 h and cooled naturally, before the XRD experiment. The crystallite grain size (D_t) of HEFOA was estimated by using the Scherrer formula in eqn (6):[57]

$$D_t = 0.89 \frac{\lambda}{\beta \cos \theta} \tag{6}$$

where λ is the wavelength of XR radiation, β is the corrected peak width at half-maximum intensity (FWHM in radians), and θ is the peak position of the main reflection.

Calculation of sintering activation energy. The grain growth process during isothermal annealing can be described by combining a generalized grain growth equation with the Arrhenius relationship using eqn (7):[58]

$$D^n - D_0^n = tk = tk_0 \exp(-Q_g/RT) \tag{7}$$

D is the grain size after annealing time t, D_0 is the initial grain size, n is the grain growth exponent ($n = 2$ in this study), t is the annealing time (held constant at 4 h for all measurements), k_0 is a pre-exponential constant, Q_g is the sintering activation

energy, R is the universal gas constant, and T is the absolute temperature.

STEM-HAADF and elemental mapping were performed using an aberration-corrected JEOL ARM 200CF operated at 200 kV and 80 kV, equipped with an Oxford Instruments XEDS system. Complementary bright-field TEM imaging. SAED and XEDS analyses were conducted on a JEOL JEM-2800 microscope (200 kV) equipped with a JEOL EDS detector featuring 100 mm² silicon drift detectors (SDDs) and a solid collection angle of ~ 0.95 sr. Gaussian peak fitting was employed to deconvolute overlapping Pt L, Ta L, and Er L lines, while a linear function was used for background subtraction. Minor peaks of Ta and Er were included based on their known relative intensities with respect to the corresponding Lα peaks.

TG-DSC curve of HEFOA was recorded by a thermogravimetric analyzer (STA 449F3, NETZSCH, Germany) under atmospheric conditions and a heating ramp rate of 10 °C min^{-1}.

The BET specific surface areas and N$_2$ adsorption isotherms were determined using a Micromeritics 3 Flex adsorption analyzer after degassing the sample for 12 h at 200 °C in N$_2$.

XPS measurements were performed using the ESCALAB 250 device of thermo electron with a monochromatic ray Al Kα (1486.6 eV) as the excitation source. The O 1s binding energy scale was calibrated using the C 1s reference peak from adventitious carbon, standardized at 284.8 eV.

The *in situ* CO-DRIFTS analysis was conducted using a Nicolep iS50 instrument. The sample was reduced at 300 °C for 60 minutes by 5 vol% H$_2$/N$_2$ at first, and then cooled down to 30 °C to obtain the background spectrum in Ar. Subsequently, the spectrum was collected when the 5 vol% CO/N$_2$ was opened, finally changed to Ar after adsorption of CO for 15 min. All the spectra were recorded by accumulating 64 scans at a resolution of 4 cm^{-1}.

In situ DRIFTS of catalytic NH$_3$ combustion showing the reactivity of adsorbed NH$_3$ species with 3 vol% O$_2$/Ar at 250 °C. The sample was treated at 250 °C for 60 minutes by 20 ml min^{-1} Ar to remove surface impurities at first, and then obtained the background spectrum at 250 °C in Ar. Then, 2 vol% NH$_3$/Ar (100 ml min^{-1}) was flowed into the sample holder for 30 minutes and changed to a rate of 20 ml min^{-1} Ar for another 20 minutes. Finally, the 3 vol% O$_2$/Ar (100 ml min^{-1}) was introduced to obtain the final data at 250 °C in 10 minutes. All the spectra were recorded by accumulating 64 scans at a resolution of 4 cm^{-1}.

Author contributions

Q. H., Y. D. and L. X. conceived the project. Y. D., co-supervised by Q. H. and N. Y., L. X., co-supervised by Q. H. and H. W. conducted most of the experiments including synthesis, characterization, and testing, as well as data analysis. B. Y., supervised by Q. H. carried out STEM and TEM characterization of the catalysts and prepared the relevant part of the manuscript. X. H. assisted in materials synthesis. C. X. assisted in materials characterization. Z. D. assisted in the data analysis. Y. D., L. X., B. Y., and Q. H. drafted the paper. Q. H. and N. Y. revised the paper. All authors discussed the paper.

Conflicts of interest

The authors declare no competing interests.

Data availability

The data supporting the findings of this study are available from the corresponding author (heqian@nus.edu.sg) upon reasonable request. Additional supporting data are provided in the SI. The supplementary information contains additional experimental details and characterization data (TEM, STEM, SEM, TGA, *in situ* DRIFTS, XRD, *etc.*), presented in supplementary figures (S1–S19) that support the findings of this study. See DOI: **https://doi.org/10.1039/d5nh00411j**

Acknowledgements

References

1 A. Valera-Medina, H. Xiao, M. Owen-Jones, W. I. F. David and P. J. Bowen, *Prog. Energy Combust. Sci.*, 2018, **69**, 63–102.

2 S. Hinokuma, Y. Kawabata, S. Matsuki, H. Shimanoe, S. Kiritoshi and M. Machida, *J. Phys. Chem. C*, 2017, **121**, 4188–4196.

3 K. S. Indriadi, Y. Du, Q. He and N. Yan, *Appl. Energy*, 2025, **393**, 126099.

4 K. Qian, Y. Wu, C. Chen, L. Zou, Y. Cui and D. Liu, *J. Energy Inst.*, 2025, **119**, 101979.

5 X. Su, C. Li, J. Chen, T. Tang, J. Xue, Y. Chen, V. Rac, V. Rakić and X. Du, *Mol. Catal.*, 2024, **562**, 114224.

6 M. Yu, R. Sun, G. Luo, L. Wang, X. Li and H. Yao, *Fuel*, 2024, **367**, 131306.

7 S. Hinokuma and K. Sato, *Chem. Lett.*, 2021, **50**, 752–759.

8 S. Hinokuma, T. Iwasa, K. Araki, Y. Kawabata, S. Matsuki, T. Sato, Y. Kon, T. Taketsugu, K. Sato and M. Machida, *J. Jpn. Pet. Inst.*, 2020, **63**, 274–281.

9 S. Hinokuma, K. Araki, T. Iwasa, S. Kiritoshi, Y. Kawabata, T. Taketsugu and M. Machida, *Catal. Commun.*, 2019, **123**, 64–68.

10 Y. Wu, J. Mei, T. Cai, W. Wang, H. Zhu, T. Sun and D. Liu, *Combust. Flame*, 2022, **237**, 111845.

11 G. Zhou, Y. Zhang, X. Zhao, Y. Gui, X. Wang, L. Li, T. Chen, Z. Huang and H. Lin, *Fuel*, 2023, **334**, 126824.

12 B. Cui, Y. Wang, S. Zhou, R. Ruan, H. Tan and X. Wang, *Fuel*, 2024, **378**, 132831.

13 P. J. F. Harris, *J. Catal.*, 1986, **97**, 527–542.

14 Z. Huang, T. Ban, Y. Zhang, L. Wang, S. Guo, C.-R. Chang and G. Jing, *Appl. Catal., B*, 2021, **283**, 119625.

15 E. M. Slavinskaya, L. S. Kibis, O. A. Stonkus, D. A. Svintsitskiy, A. I. Stadnichenko, E. A. Fedorova, A. V. Romanenko, V. Marchuk, D. E. Doronkin and A. I. Boronin, *ChemCatChem*, 2021, **13**, 313–327.

16 Y. Du, B. Yao, L. Xu, S. Lu, C. Xu, P. Han, S. Dai, S. Wang, S. Xi, B. S. Neo, N. Yan and Q. He, *Joule*, 2025, 102030.

17 J. Lee, H. Jeon, D. G. Oh, J. Szanyi and J. H. Kwak, *Appl. Catal., A*, 2015, **500**, 58–68.

18 S. Shabani, M. Jamalpour, S. M. Mirkazemi and S. Trasatti, *Ceram. Int.*, 2025, **51**(18), 25508–25519.

19 S. Jang, D. Gun Oh, H. Kim, K. Hyun Kim, K. Khivantsev, L. Kovarik and J. Hun Kwak, *Angew. Chem., Int. Ed.*, 2024, **63**, e202400270.

20 A. Aitbekova, C. Zhou, M. L. Stone, J. S. Lezama-Pacheco, A.-C. Yang, A. S. Hoffman, E. D. Goodman, P. Huber, J. F. Stebbins, K. C. Bustillo, P. Ercius, J. Ciston, S. R. Bare, P. N. Plessow and M. Cargnello, *Nat. Mater.*, 2022, **21**, 1290–1297.

21 H. Xu, Z. Zhang, J. Liu, C.-L. Do-Thanh, H. Chen, S. Xu, Q. Lin, Y. Jiao, J. Wang, Y. Wang, Y. Chen and S. Dai, *Nat. Commun.*, 2020, **11**, 3908.

22 X. Ping, Q. Yang, B. Meng, Z. Ma and X. Pan, *J. Alloys Compd.*, 2024, **975**, 172971.

23 L. Sun, K. Wen, G. Li, X. Zhang, X. Zeng, B. Johannessen and S. Zhang, *ACS Mater. Au*, 2024, **4**, 547–556.

24 L. Sun, J. A. Yuwono, S. Zhang, B. Chen, G. Li, H. Jin, B. Johannessen, J. Mao, C. Zhang, M. Zubair, N. Bedford and Z. Guo, *Adv. Mater.*, 2024, **36**, 2401288.

25 J. Hou, Y. Liu, C. Cheng, F. Cheng, P. Qin, Y. Miao, W. Ji and X. Wang, *J. Alloys Compd.*, 2024, **996**, 174774.

26 S. L. Liew, X. P. Ni, F. Wei, S. Y. Tan, M. T. Luai, P. C. Lim, S. L. Teo, N. B. M. Rafiq, J. Zhou and S. Wang, *J. Eur. Ceram. Soc.*, 2022, **42**, 6608–6613.

27 Y. Li, K. Wang, X. Wang, Z. Wang, J. Xu, M. Zhao, X. Wang, S. Song and H. Zhang, *Chin. J. Catal.*, 2024, **61**, 54–70.

28 F. Okejiri, J. Fan, Z. Huang, K. M. Siniard, M. Chi, F. Polo-Garzon, Z. Yang and S. Dai, *iScience*, 2022, **25**(5), 104214.

29 S. Fang, T. Yang, W. He, W. Yang, N. Wang, S. Ma, K. Shih and C. Liao, *Ceram. Int.*, 2024, **50**, 7431–7440.

30 Y. Gao, M. Zhang, Y. Mao, H. Cao, S. Zhang, W. Wang, C. Sun, Z. Song, J. Sun and X. Zhao, *Energy Convers. Manage.*, 2022, **252**, 115125.

31 Q. Huang, C. Yin, Y. Lei, Y. Fang, H. Wang, H. Wu, H. Luo, Y. Xu, Y. Wang, Y. Miao and H. Wang, *Sep. Purif. Technol.*, 2025, **359**, 130672.

32 L. Xu, M. Niu, L. Su, X. He, H. Ni, H. Gao, L. Zhuang and H. Wang, *Corros. Sci.*, 2024, **227**, 111682.

33 C. Liu, S. Li, Y. Zheng, M. Xu, H. Su, X. Miao, Y. Liu, Z. Zhou, J. Qi, B. Yang, D. Chen, C.-W. Nan and Y.-H. Lin, *Prog. Mater. Sci.*, 2025, **148**, 101385.

34 D. Lu, H. Wang, L. Su, M. Niu, P. Guo, H. Gao, L. Zhuang, Z. Cai and L. Xu, *J. Am. Ceram. Soc.*, 2022, **105**, 2783–2790.

35 G. Chen, C. Li, H. Jia, H. Li, S. Li, B. Gong, L. An and K. Chen, *J. Eur. Ceram. Soc.*, 2023, **43**, 2586–2592.

36 Y. Pan, J.-X. Liu, T.-Z. Tu, W. Wang and G.-J. Zhang, *Chem. Eng. J.*, 2023, **451**, 138659.

37 S. S. Aamlid, M. Oudah, J. Rottler and A. M. Hallas, *J. Am. Chem. Soc.*, 2023, **145**, 5991–6006.

38 R. Song, G. Zhao, J. M. Restrepo-Flórez, C. J. Viasus Pérez, Z. Chen, C. Ai, A. Wang, D. Jing, A. A. Tountas, J. Guo, C. Mao, C. Li, J. Shen, G. Cai, C. Qiu, J. Ye, Y. Fu, C. T. Maravelias, L. Wang, J. Sun, Y.-F. Xu, Z. Li, J. Y. Y. Loh, N. T. Nguyen, L. He, X. Zhang and G. A. Ozin, *Nat. Energy*, 2024, **9**, 750–760.

39 M. Zhang, Y. Gao, C. Xie, X. Duan, X. Lu, K. Luo, J. Ye, X. Wang, X. Gao, Q. Niu, P. Zhang and S. Dai, *Nat. Commun.*, 2024, **15**, 8306.

40 M. Zhang, X. Duan, Y. Gao, S. Zhang, X. Lu, K. Luo, J. Ye, X. Wang, Q. Niu, P. Zhang and S. Dai, *ACS Appl. Mater. Interfaces*, 2023, **15**, 45774–45789.

41 Y. Liu, C. Ye, L. Chen, J. Fan, C. Liu, L. Xue, J. Sun, W. Zhang, X. Wang, P. Xiong and J. Zhu, *Adv. Funct. Mater.*, 2024, **34**, 2314820.

42 J. Cheng, N.-X. Ci, H.-Q. Zhang, Z. Zeng, X. Zhou, Y.-Y. Li, H.-J. Qiu, W. Zhai, D.-D. Gao, L.-J. Ci and D.-P. Li, *Rare Met.*, 2025, **44**, 961–972.

43 L. Su, X. Chen, L. Xu, T. Eldred, J. Smith, C. DellaRova, H. Wang and W. Gao, *ACS Nano*, 2022, **16**, 21397–21406.

44 H. Cai, P. Zhang, B. Li, Y. Zhu, Z. Zhang and W. Guo, *Mater. Today Catal.*, 2024, **4**, 100039.

45 C. M. Rost, E. Sachet, T. Borman, A. Moballegh, E. C. Dickey, D. Hou, J. L. Jones, S. Curtarolo and J.-P. Maria, *Nat. Commun.*, 2015, **6**, 8485.

46 S. Lee, J. Seo and W. Jung, *Nanoscale*, 2016, **8**, 10219–10228.

47 J. Chen, S. Xiong, H. Liu, J. Shi, J. Mi, H. Liu, Z. Gong, L. Oliviero, F. Maugé and J. Li, *Nat. Commun.*, 2023, **14**, 3477.

48 M. J. Hülsey, S. Baskaran, S. Ding, S. Wang, H. Asakura, S. Furukawa, S. Xi, Q. Yu, C.-Q. Xu, J. Li and N. Yan, *CCS Chem.*, 2022, **4**, 3296–3308.

49 B. Qiao, A. Wang, X. Yang, L. F. Allard, Z. Jiang, Y. Cui, J. Liu, J. Li and T. Zhang, *Nat. Chem.*, 2011, **3**, 634–641.

50 T. Lan, M. Gao, J.-Y. Hasegawa, Y. Shen, W. Qu, Q. Hu, J. Deng, D. Cheng and D. Zhang, *ACS Catal.*, 2023, **13**, 14070–14079.

51 W. Tan, S. Xie, X. Zhang, K. Ye, M. Almousawi, D. Kim, H. Yu, Y. Cai, H. Xi, L. Ma, S. N. Ehrlich, F. Gao, L. Dong and F. Liu, *ACS Appl. Mater. Interfaces*, 2024, **16**, 454–466.

52 H. Sun, H. Wang and Z. Qu, *ACS Catal.*, 2023, **13**, 1077–1088.

53 J. G. Amores, V. S. Escribano, G. Ramis and G. Busca, *Appl. Catal., B*, 1997, **13**, 45–58.

54 G. Ramis, L. Yi and G. Busca, *Catal. Today*, 1996, **28**, 373–380.

55 W. Tan, Y. Cai, H. Yu, S. Xie, M. Wang, K. Ye, L. Ma, S. N. Ehrlich, F. Gao, L. Dong and F. Liu, *Environ. Sci. Technol.*, 2023, **57**, 15747–15758.

56 A. Abd El-Moemen, A. M. Abdel-Mageed, J. Bansmann, M. Parlinska-Wojtan, R. J. Behm and G. Kučerová, *J. Catal.*, 2016, **341**, 160–179.

57 A. Monshi, M. R. Foroughi and M. R. Monshi, *World J. Nano Sci. Eng.*, 2012, **2**, 154–160.

58 Q. Li and X. Jiao, *Materialia*, 2019, **5**, 100188.